Submitted March 2022 to Journal of Physical Oceanography.

Interpretation of net surface heat fluxes and Meridional Overturning Circulations in global coupled UK-HadGEM3 climate simulations

Michael J. Bell[a], A. J. George Nurser[b], and David Storkey[a]

[a] *Met Office, Exeter, EX1 3PB, UK*
[b] *National Oceanography Centre, University of Southampton Waterfront Campus, Southampton, UK*

ABSTRACT: The annual mean net surface heat fluxes (NSHFs) from the ocean to the atmosphere play an important role in driving both atmospheric circulations and oceanic meridional overturning circulations. Those generated by historical forcing simulations using the UK HadGEM3-GC3.1 coupled climate model are shown to be relatively independent of resolution, for model horizontal grid spacings between 1° and $1/12^\circ$, and to agree well with those based on the DEEPC analyses for the period 2000–2009. Interpretations of the geographical patterns of the NSHFs are suggested that are based on relatively simple dynamical ideas. As a step toward investigation of their validity, we examine the contributions to the rate of change of the active tracers (potential temperature, salinity and potential density) from the main terms in their prognostic equations as a function of the active tracer and latitude. We find that the main contributions from vertical mixing occur in "near surface" layers and that, except at high latitudes, the time-mean advection of potential temperature and density is well anti-correlated with the sum of the surface fluxes and vertical diffusion. By contrast, the tracer budget for the salinity has at least four terms of comparable magnitude. The heat input by latitude bands is shown to be dominated by the NSHFs, the time-mean advection, and the equatorial Pacific. Expressions for global integrals of the salt and heat content tendencies due to advection as a function of salinity and potential temperature respectively are derived and shown to make contributions that should not be neglected.

SIGNIFICANCE STATEMENT: Our aim is to understand better how the heat and freshwater that are input into the ocean from the atmosphere are then redistributed within the ocean and released back into the atmosphere. We show that the geographical patterns of the heat that is input to or released from the ocean surface in coupled climate models agree well with observations. We outline a dynamically-based interpretation of these surface fluxes and provide evidence that supports some of its assumptions. This work might in future help us to understand how the patterns of the surface fluxes will respond to changes in green-house gas forcing.

1. Introduction

Meridional overturning cells are a key component of the ocean circulation (Gordon 1986; Broecker 1991; Talley et al. 2011). How these cells are driven by surface winds and relate to surface fluxes of heat and moisture is still a very active area of research (see e.g. Srokosz et al. 2021). These surface fluxes of heat and moisture also play an important role in driving atmospheric circulations such as the mid-latitude weather systems (Minobe et al. 2008; Hewitt et al. 2017). Changes due to greenhouse gas forcing in the surface heat fluxes and the meridional overturning cells are intimately related to ocean heat uptake, an issue of enormous societal importance and intensive study (Gregory et al. 2016; Fox-Kemper et al. 2021).

Corresponding author: Michael J. Bell, mike.bell@metoffice.gov.uk

The dynamics of the time-mean meridional overturning circulations (MOCs) are complicated by many factors. For example: the circulations in the three main ocean basins (Atlantic, Indian and Pacific) are significantly different and interact through the Southern Ocean and Indonesian Through Flow; there are upper, middle and lower MOC cells; some of these cells interact with the gyre circulations (see section 2c); salinity variations play a major role in the middle and lower cells with the density of water at very high latitudes more dependent on its salinity than its temperature (Huang 2010; Talley et al. 2011); analysis of the energetics of MOCs suggests that wind forcing plays a more important role than internal mixing in driving MOCs (Vallis 2017) but some aspects of the energetics are quite subtle (Gnandesikan et al. 2005); there is evidence that mesoscale motions, particularly in the Southern Ocean, play an important role in determining the strength of the mid-depth cells at least in some configurations (Munday et al. 2013).

Dynamically-based conceptual models (DBCMs) of time-mean MOCs, such as those of Gnandesikan (1999) and Nikurashin and Vallis (2011), have nonetheless been developed. Johnson et al. (2019) provide a recent survey of the understanding that has been gleaned from conceptual models of MOCs over the last decade. General circulation models (GCMs) are so complex that it is highly desirable to base their interpretation on diagnostics that can be related to such conceptual models. This can be useful even if the assumptions on which these conceptual models are based are not entirely valid, providing the departures from the as-

sumptions are quantified and the impact of these departures assessed.

Fields of tracer tendencies driven by the various GCM processes, including the net surface heat fluxes (NSHFs), mixing, advection etc. are powerful diagnostic tools that illuminate how the NSHFs and MOCs in the model relate to the DBCMs. Important analyses of tracer trends in (ϕ, z) space (where ϕ is latitude and z is height) have been provided by Exarchou et al. (2015); Griffies et al. (2015); Kuhlbrodt et al. (2015); Dias et al. (2020); Saenko et al. (2021). Much of that work focuses on global budgets (as a function of z only), but Griffies et al. (2015); Dias et al. (2020) in particular also assess spatial patterns of the terms. The theory and literature on the diagnosis of water mass transformations (WMT), following the ideas of Walin (1982), where the focus is on isothermal (or isohaline or isopycnal layers), has recently been reviewed by Groeskamp et al. (2019). The analysis of Nurser et al. (1999) is particularly relevant to our discussion as it draws attention first to the relationship between Ekman upwelling velocity and water mass transformation rates in regions where the ocean is absorbing heat and second to the question of whether vertical mixing is dominated by that related to the surface mixed layer (i.e. inside or just outside the mixed layer) or that lower down in the ocean interior. The latter is also addressed for the Southern Ocean by Tamsitt et al. (2018). The surface streamfunction approach of Marsh (2000) and Grist et al. (2014) also has similarities to our approach.

The first of the two main aims of this paper is to propose an interpretation of the NSHFs generated by the HadGEM3 atmosphere-ocean coupled GCM that is based on a DBCM of the MOC. The second aim is to start to investigate the validity of the assumptions of the DBCM using tracer trend diagnostics from the GCM. The DBCM of the MOC is a generalisation of that derived in Schloesser et al. (2012), Bell (2015b) and Bell (2015a).

We first validate in section 2b the NSHFs in the HadGEM3 coupled climate models of 1° to 1/12° resolution by comparing them with the DEEPC estimates of the NSHFs (Liu et al. 2015) for the period 2000-2009. These DEEPC estimates are much more reliable than previous products (Hyder et al. 2018). We show that the HadGEM3 NSHFs agree well with those of DEEPC and that in most regions they are relatively insensitive to the model resolution. Subsection 2c presents our interpretation of these NSHFs and the associated MOCs in terms of our DBCM. Our interpretation suggests that Ekman upwelling is a key element in regions of net surface heat input to the ocean. It also supposes that advection by the time-mean flow is a key element in regions of heat loss to the atmosphere.

Section 3 investigates diagnostics of the terms in the prognostic equation for potential temperature. The results are intended to provide both qualitative and quantitative information on to what extent and in what regions our assumptions are valid. These diagnostics are calculated as a function of potential temperature class, θ, and latitude, ϕ, for individual ocean basins, and presented in (ϕ, θ) space rather than (ϕ, z) space (Lee et al. 2002). In common with several other authors (Nurser et al. 1999; Iudicone et al. 2008a; Hieronymus and Nycander 2013; Groeskamp et al. 2018) we find that solar penetration makes an appreciable difference to the distribution across the temperature classes of the heat input by the penetrating and non-penetrating "surface" heat fluxes. As the DBCM considers water mass transformations in density space, we also present corresponding calculations for salinity, s, and potential density, ρ, classes.

Section 3a describes the diagnostics. Section 3b investigates the contributions from absorption of surface fluxes and vertical diffusion with a focus on the latter. We argue that the vertical diffusion contributions are largely confined to the upper ocean. Section 3c considers the contributions from advection and isopycnal diffusion in balancing contributions from other terms. We show to what extent the mean advection is correlated with the inputs from the surface fluxes. Section 3d considers the contributions to heat and salinity tendencies by tracer class summed over all latitudes and basins. The advection terms are expected to be close to zero. Departures from zero, derived in the appendix, are shown to be non-negligible for both salinity and heat. Section 3e considers the contributions to the heat content summed over tracer classes within broad latitude bands and investigates the sources of the heat lost in the north Atlantic. Section 4 summarises our conclusions and briefly discusses potential further work.

2. Net surface heat fluxes

a. Description of the data

The HadGEM3-GC3.1 coupled atmosphere-land-ice-ocean model configurations and integrations used in this study are described in Roberts et al. (2019), R19 hereafter. Kuhlbrodt et al. (2018) describes the details of the NEMO ORCA1 (L) ocean model configuration and Storkey et al. (2018) describes the details for the ORCA025 (M) and ORCA0083 (H) configurations. The letters L, M and H denote low, medium and high resolution, the configurations respectively having 1°, 1/4° and 1/12° zonal grid spacing at the equator. R19 similarly denote their atmosphere-land configurations by the letters L, M and H, the mid-latitude grid spacing being respectively 135, 60 and 25 km. We use the coupled configurations denoted by LL, MM and HH, the first letter indicating the atmosphere and the second the ocean configuration. In these configurations very few parameters explicitly depend on the grid resolution of the atmosphere or the ocean model. However the representation of the ocean mesoscale in the L configuration is largely parametrised whilst in the M and H configurations

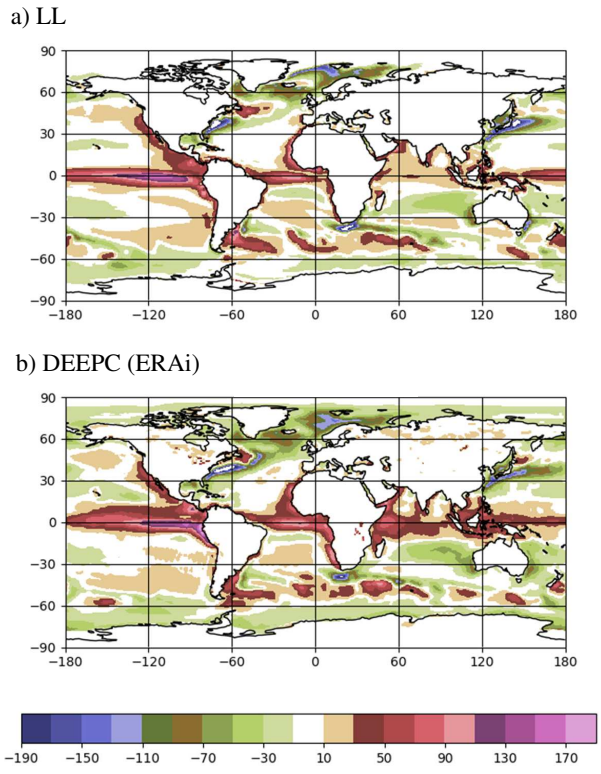

FIG. 1. Annual mean NSHF (Wm^{-2}) for the period 2000–2009 calculated (a) from an ensemble of eight CMIP6HiResMIP N96 ORCA1 hist-1950 simulations and (b) using the DEEPC methodology with ERA interim fluxes as input.

it is increasingly represented explicitly (at least at lower latitudes). As described in Storkey et al. (2018), the representation of eddy-induced fluxes (Gent and McWilliams 1990) is only used in the L configuration and the isopycnal diffusion coefficient is set equal to 1000, 150 and 125 m^2s^{-1} in the L, M and H configurations respectively. Vertical mixing of tracers is parametrised using a modified form of the Gaspar et al. (1990) TKE scheme and a background vertical eddy diffusivity of $1.2\times10^{-5}m^2s^{-1}$ (see Storkey et al. 2018, for details).

We use the integrations referred to by R19 as control-1950 and hist-1950. Control-1950 uses forcing data sets (for solar heating, greenhouse gases, aerosols etc) representing conditions in the 1950s whilst hist-1950 uses forcing representing historic conditions from 1950-2014. Both of these integrations start after a 30-year spin-up using the 1950s forcing. The initial conditions for the spin-up are the January 1950-1954 mean EN4 ocean analysis (Good et al. 2013) and the ERA-20C in January 1950 (see R19 for more detail).

The DEEPC NSHFs (Liu et al. 2015) are derived from reconstructions of the net radiation at the top of the atmosphere calculated using measurements from the CERES satellite and energy flux divergences calculated from atmospheric re-analyses. We focus mainly on the products derived using ERA-interim re-analyses but present also one figure using fluxes calculated using MERRA re-analyses. Liu et al. (2017) provide evaluations of the accuracy of these fluxes and Hyder et al. (2018) supplementary figure 1 shows that these DEEPC estimates are much more reliable than previous products.

Diagnostics for the Pacific, Atlantic and Indian oceans have been calculated using the "standard" basin masks for each configuration. These masks have been extended into the Southern Ocean taking the boundaries between the basins to lie at 25°E, 135°E and 70°W.

b. Comparison of model and DEEPC net surface heat fluxes

Figure 1 compares annual mean NSHFs for the period 2000-2009 calculated using an 8-member ensemble of LL hist HadGEM3-GC3.1 integrations and the DEEPC monthly products based on ERA-interim reanalyses. The patterns and magnitudes of the two sets of NSHFs are generally in good agreement. The strong net surface heating regions agree well in: the eastern equatorial Pacific; the equatorial Atlantic; the south Atlantic and south-western Indian Ocean (between 45° and 60°S); and on the eastern boundaries of the Atlantic and Pacific, particularly in the northern hemisphere to the west of Africa and the American continent. The strong net surface cooling regions agree well in the north Atlantic and south of 60°S, and in the western boundary current extensions of the Gulf Stream, Kuroshio, east Australian current, Brazil current and the Agulhas retroflection. There are also several other regions of weaker surface fluxes where the agreement is qualitatively good and the large region of surface heat loss in the eastern Indian Ocean between the equator and 30°S also agrees well.

Figure 2(a) shows the difference between the fluxes presented in figure 1. Parts (b) and (c) of the figure present the corresponding differences for 3- and 4-member ensembles of the MM and HH hist integrations respectively. The largest differences between these three plots are in the north-west Atlantic where the positive difference progressively reduces as the model resolution improves. This reflects an improvement in the path of the Gulf Stream to the east of the Grand Banks which results in a notorious cold bias in the LL model (and most other climate models of comparable resolution). The differences in the Agulhas retroflection region for the HH simulation are also smaller than those for the other simulations. In most other regions the differences between the NSHFs are relatively independent of model resolution. In particular there are some large resolution-independent biases just north of the equator and west of 120°W in the Pacific and just south of the equator around 60°E in the Indian ocean. This may be because the atmosphere model does not resolve tropical convection

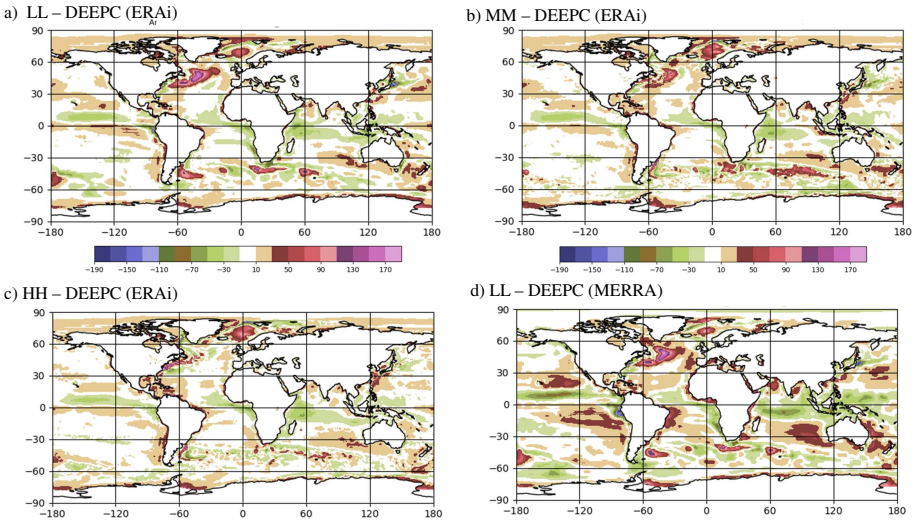

FIG. 2. Annual mean NSHF for the period 2000–2009 from hist-1950 coupled climate model integrations minus that calculated using the DEEPC methodology with ERA-interim fluxes as input for ensembles of (a) an 8-member N96 ORCA1 ensemble (b) a 4-member N216 ORCA025 ensemble and (c) a 3-member N512 ORCA0083 ensemble. (d) same as (a) except that the DEEPC methodology used MERRA fluxes as input.

cells in any of the configurations. Or it might be due to inaccuracies in the DEEPC product. (Inter-decadal variations in the model heat fluxes are significantly smaller than these biases.) Figure 2(d) shows the difference between the LL fluxes and those for 2000–2009 from the DEEPC product calculated using the MERRA re-analyses. One clearly sees that the differences in (d) are generally larger than those in (a).

Panels (a)–(d) of Figure 3 display the net heat input by latitude band calculated from DEEPC ERAi and the LL, MM and HH control integrations for the decade 2000-2009. There is generally good qualitative and quantitative agreement between all four products. The Pacific dominates the heat input in the equatorial band between 15°S and 15°N in all the products, being at least twice as large as the heat input in the Atlantic and Indian Oceans combined. We note also that DEEPC has the largest and MM the smallest heat input in the equatorial Pacific band, and the LL integration loses least heat from the Atlantic between 30°N and 60°N. We return to this figure in section 3e.

c. Linking net surface heat fluxes to MOC

Gnandesikan (1999) proposed a DBCM of the middle MOC cell which was motivated by the idea that this cell "connects" the region of heat loss in the north Atlantic to that of heat gain in the Southern Ocean. Bell (2015a) aimed to explain why, in agreement with the NSHF products available at the time, this heat gain in the Southern Ocean is focused on the south Atlantic and south-western Indian Ocean. His DBCM was based on somewhat complicated calculations using the planetary geostrophic equations which aimed to apply the techniques developed with great success by Luyten et al. (1983) for the ventilated thermocline to describe MOCs. These calculations cannot be used directly to diagnose GCM output because they are limited to models with small numbers of vertical layers and relatively simple forcing scenarios. Some key ideas can nonetheless be distilled from these calculations and used to interpret the GCM outputs. These ideas are explained in this subsection with the assistance of figures 4 and 5.

The first idea is that the depths of potential density, or neutral density, isopycnals should be relatively independent of latitude along the eastern boundaries and some sections of the western boundaries of each of the major ocean basins. This expectation is based on the condition of no normal flow at the boundary and our knowledge of boundary waves (Marshall and Johnson 2013). There is evidence that this is a good approximation in GCMs, at least within about 40° to 50° of the equator, but the details deserve separate publication. Hughes et al. (2018) present an extensive study of the related issue of bottom pressure variations along the ocean boundaries. Where the ocean potential density is primarily determined by the potential temperature (again within about 40° to 50° of the equator) this implies that the near surface temperature will be relatively independent of latitude compared with the atmospheric surface temperature.

The second idea is that in regions where there is a sustained (i.e. time-mean) NSHF into the ocean, there must be a compensating provision of cold water to the surface and that this is most likely to be supplied by Ekman upwelling of cold water from below (or equatorward transport by Ekman transports). Along the equatorial Pacific (and

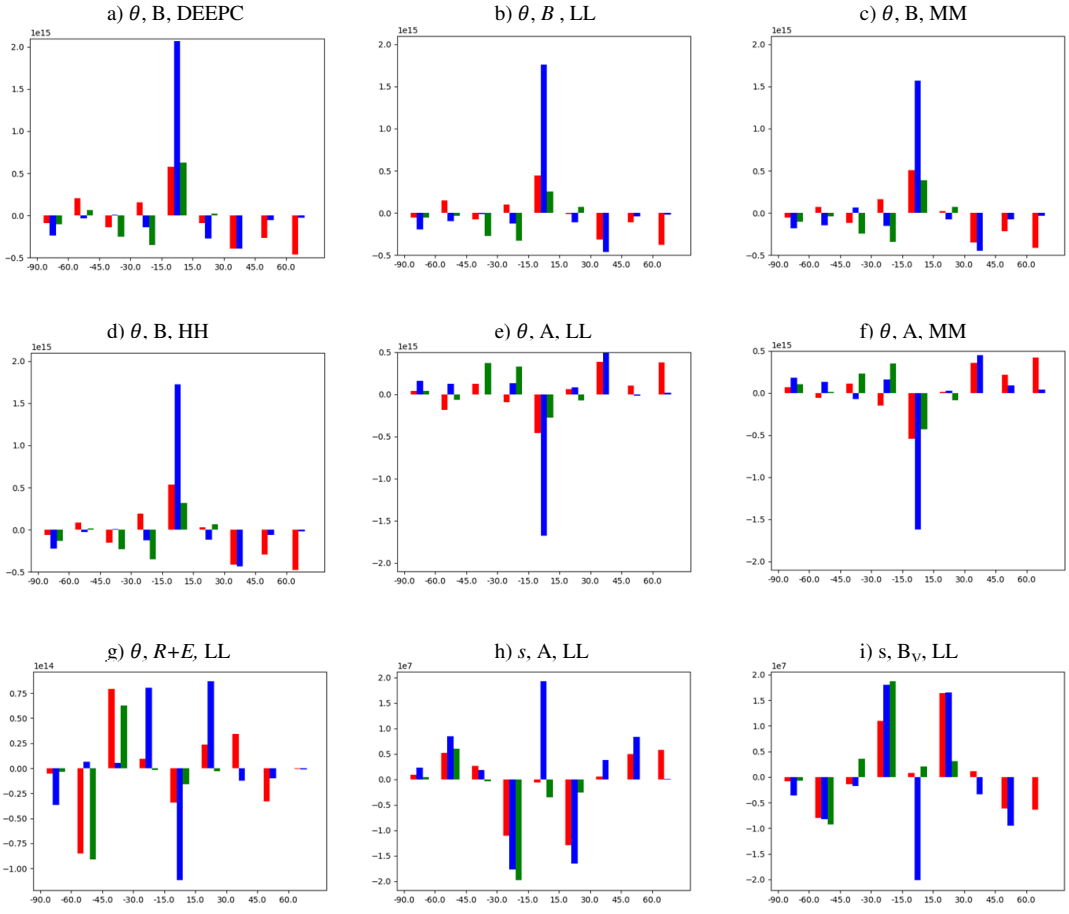

FIG. 3. (a) - (d) Net surface heat flux (W) by latitude band and ocean basin (red Atlantic, blue Pacific and green Indian ocean) according to (a) DEEPC and (b) to (d) the LL, MM and HH pre-industrial control simulations respectively. Heat flux by the Advection (W) from (e) the LL and (f) the MM control simulations. (g) As in (e) but for the Residual advection and Eddy-induced advection $R+E$. Salinity flux (kgs^{-1} in the LL control simulations by (g) Advection and (h) virtual surface salt flux. All figures use data for the period 2000-2009.

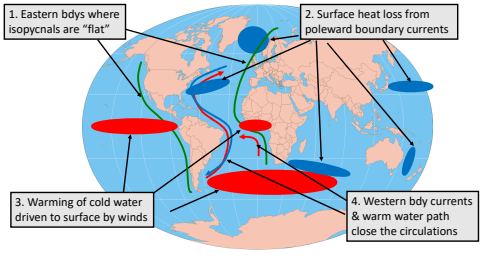

FIG. 4. Schematic describing how the main geographical patterns of the NSHF can be inferred from relatively simple dynamical processes.

Atlantic) it is well known that prevailing winds from the east cause the thermocline that is deep in the west of the basin to shoal in the east. The upwelling at the equator is very strong because there is a strong poleward Ekman transport on both sides of the equator at about 3° to 5° from the equator. Where relatively cold water is upwelling and being converted into warmer water by the surface fluxes, the rate of water mass transformation must be equal to the upwelling velocity (Nurser et al. 1999; Bell 2015a).

The third idea, based on Gnandesikan (1999), is that, in a steady state, the total rate at which a water mass is being formed must be the same as the rate at which it is being destroyed (i.e. converted into other water masses). The rates of water mass formation and destruction will depend on the depths of the layers, and the depths of the layers are largely determined by the condition that their rate of formation and destruction be equal. The warm water formed by Ekman upwelling and net surface heating in the eastern equatorial

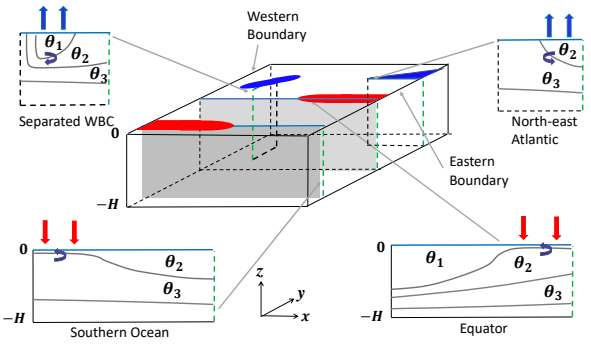

FIG. 5. Schematic depicting vertical cross-sections through an ocean with three active layers of water of different potential temperatures (θ_1 to θ_3). Net surface heating and cooling (thick red and blue arrows) transform cooler to warmer water and warmer to cooler water respectively (purple arrows). The regions of heat uptake are associated with Ekman upwelling and the regions of heat loss with poleward advection of the upper layer. The ocean has one square-shaped basin with due north-south eastern and western boundaries solely to simplify its presentation.

Pacific (and Atlantic) will accumulate on the western side of the basin and spread poleward at least along a section of the western boundary (in which the isopycnals are relatively flat). We expect some of this water to be entrained in the subtropical gyre circulations and to be exported poleward by the western boundary currents. These currents that are relatively warm compared to the atmosphere are then expected to provide a significant source of heat (and moisture) to the atmosphere.

The fourth and final idea is that the surface and deep western boundary currents are able to complete the circulations required to return the water masses transferred between layers by the transformations associated with the surface fluxes.

Figure 4 indicates how these ideas can be applied to account for some of the most significant patterns of surface heat flux evident in figure 1. It is suggested in Bell (2015a) that the poleward flow into the north-east Atlantic is due to an eastern boundary current (the Norwegian coastal current) associated with the relatively warm water at high latitudes on the eastern boundary and that the lack of a similar heat loss in the Pacific is associated with the fresh surface salinities in the north Pacific emphasised in the description of ocean properties by Huang (2010). The location of the region of surface heating in the south Atlantic and south-west Indian Ocean (Box 3 in Fig. 4; see also Fig. 1) relates to the westward outcropping of water in a sub-polar gyre, treating the region north and west of Drake passage as a sub-polar gyre that extends right around the globe (see also Stommel 1957; Marshall et al. 2016; Tamsitt et al. 2016). The regions of surface heating on the west coasts of Africa and north America mentioned earlier are presumably related to coastal Ekman upwelling.

Figure 5 provides some schematic vertical cross-sections, along the equatorial Pacific (or Atlantic), across the path of the Kuroshio (or Gulf Stream), just north of the Drake passage and in the north-east Atlantic. It emphasises the water mass transformations (purple arrows) related to Ekman upwelling and surface cooling, or to poleward advection and surface cooling. The MOCs induced by these water mass transformations, being influenced by the gyre circulations, their boundary currents and seasonal variations, can be expected to have complex (chaotic) Lagrangian trajectories, the mixing being further enhanced by mesoscale structures in frontal regions (Iudicone et al. 2008b; Tamsitt et al. 2018; van Sebille et al. 2018).

Although there is nothing particularly new or surprising in the ideas described above, their combination in this form seems to be somewhat novel and should be regarded with caution. In particular it is not yet clear to what extent these ideas are valid or helpful for assessing GCMs. The following section begins to explore these issues.

3. Tracer trend diagnostics

The data used in this section are monthly means from control integrations for the ten-year period 2000-2009.

a. Methods used to calculate tracer trend diagnostics

The NEMO code used in this study is couched in s coordinates in which cell thicknesses are allowed to change with time. Our integrations used z^* coordinates (Roullet and Madec 2000; Adcroft and Campin 2004), a particular choice of s coordinates. In s coordinates a model tracer cell is referred to by its pseudo-zonal index i, pseudo-meridional index j, and depth index k. Its vertical thickness, e_3, may depend on all these indices and vary in time, $e_3(i,j,k,t)$, whilst its pseudo-zonal width $e_1(i,j)$ and pseudo-meridional width $e_2(i,j)$ do not depend on k or t. The volume-integrated tendency T_{ijk} for a tracer τ is given (see §A.2 of Madec et al. 2019) by:

$$T_{ijk} \equiv \frac{\partial(e_1 e_2 e_3 \tau)}{\partial t} = A_{ijk} + V_{ijk} + I_{ijk} + B_{ijk}, \quad (1)$$

where advection

$$A_{ijk} = -\frac{\partial(e_2 e_3 u\tau)}{\partial i} - \frac{\partial(e_1 e_3 v\tau)}{\partial j} - \frac{\partial(e_1 e_2 \omega\tau)}{\partial k}, \quad (2)$$

and V_{ijk}, I_{ijk} and B_{ijk} represent the tracer gain by vertical diffusion, isopycnal diffusion and absorption of radiative and turbulent fluxes respectively, while u and v represent the i- and j- velocities and ω is the upward vertical velocity with respect to the s-coordinate surface (which is itself moving).

For the Coupled Model Intercomparisoon Project (CMIP), monthly mean 3D fields of these individual terms in the prognostic equations for θ and s were generated by

accumulating them on-the-fly each time step. Each cell-integrated term in (1) for θ is multiplied by $c_p\rho_0$ (where c_p is the specific heat capacity per unit mass and ρ_0 the mean density of the Boussinesq ocean) to output cell-integrated rates of heat increase in Watts. Similarly, we multiply each salinity term by $0.001\rho_0$ to give cell-integrated rates of salt mass increase, with units kgs^{-1}. We have verified that the four processes on the rhs of (1) sum to the local rate-of-change of cell-integrated heat and salt content with good accuracy at each grid-cell.

TABLE 1. Description of the terms in the tracer prognostic equations

Symbol	Long name	Description
A	Advection	Total advection including advection by eddy-induced velocity
B_θ	Absorption	Absorption of penetrating and non-penetrating radiation and turbulent surface heat fluxes
B_V	Virtual salt flux	Virtual salt flux
E	Eddy-induced advection	Eddy-induced advection (GM flux)
I	Isopycnal diffusion	Isopycnal diffusion
M	Mean advection	Advection of the time-mean field by the time-mean flow
R	Rectified advection	An estimate of the advection of the time-varying field by the time varying flow
S	Surface absorption	Total flux through the surface all (artificially) absorbed at the surface
T	Total tendency	Rate of change of tracer calculated from the differences between the start and end of the month
V	Vertical diffusion	Vertical diffusion (including convective mixing)

To bin the heat content change into potential temperature classes, we divide the interval from -6°C to 44°C into 200 θ bins of width 0.25K, and assign the cell-integrated value of each term in each cell to the two nearest θ classes whose central values bracket the cell's monthly-mean temperature. The fraction, w, donated to one of these classes varies linearly from 1, when the grid-cell θ is the same as the central value of the class, to 0 when it equals the central value of the other class. The fraction donated to the other class is given by $1-w$. The same approach is used to allocate latitude to 180 latitude bins each of 1° width. We bin the salt content change similarly, but into 200 salinity classes of width 0.05psu and the same latitude bins as the heat terms. Our analysis focuses on these monthly mean heat and salt content trend diagnostics calculated separately for the Atlantic, Indian and Pacific ocean basins as functions of ϕ and θ (or s).

Clearly it would be preferable to assign each of the terms to their classes on every time-step (as in Hieronymus and Nycander 2013; Holmes et al. 2019a, 2021), rather than assign monthly mean terms using monthly mean values of θ. Code to achieve this is not currently available in the NEMO system however and we follow Jackson et al. (2020) and Saenko et al. (2021) in using the monthly mean data that are readily available. Daily mean surface fluxes and surface values of θ and S are available and have been found to generate results for surface fluxes that are quite similar to those generated using monthly mean data.

Table 1 summarises the terms and the names and symbols we use for them. The binned terms for the heat and salt content tendencies will be denoted by capital letters without the ijk subscript. These binned terms should satisfy

$$T = A + B + I + V. \tag{3}$$

We have also attempted to calculate the contribution to the rates of change of heat and salt contents from the time-mean advection of time-mean fields. For any field q, let us denote the monthly-mean of q by $\overline{q}$, deviations of q from $\overline{q}$ by $q' = q - \overline{q}$, and the values of τ linearly averaged onto the u, v and w faces of the tracer cell on the C-grid by τ_u, τ_v and τ_w. We have used $(\overline{u\tau_u}, \overline{v\tau_v}, \overline{w\tau_w})$, $(\overline{u}, \overline{v}, \overline{w})$ and $\overline{\tau}$ to calculate the Residual advection, R, defined as the divergence of $(\overline{u'\tau'_u}, \overline{v'\tau'_v}, \overline{w'\tau'_w})$. The Eddy-induced advection, E, is calculated similarly from the divergence of $(\overline{u_e\tau_u}, \overline{v_e\tau_v}, \overline{w_e\tau_w})$, where u_e, v_e and w_e are the eddy-induced velocities at the tracer cell faces. These calculations of R and E are only estimates because they use values at the cell faces linearly interpolated from the grid centres rather than the higher order and flux-limited values used by the advection scheme within the model. The calculations of these terms for the heat content appear to be reliable but E for salinity is noisy and we have elected not to use it. Given our definitions of A, R and E, our estimate of the tendency due to the advection of the monthly mean θ by the monthly mean flow is

$$M = A - E - R. \tag{4}$$

The NEMO code used in the integrations has a fully non-linear free surface in which evaporation and precipitation provide surface mass fluxes of freshwater (FW), expressed as a flux through the top of the uppermost grid cell. No "virtual" surface source or sink of salt such as is necessary in models with a rigid-lid is explicitly imposed in the model. There is therefore no explicit B term, and the advection term A_{ij1} of (2) effects the surface salinity changes associated with the surface FW flux through the compensating advection of saltier water through the base of the surface grid cell. However, for our diagnostics, we wish to separate out the effect of interior advection from these surface mass fluxes and we find it convenient to decompose a net freshwater outward flux (e.g. Nurser and

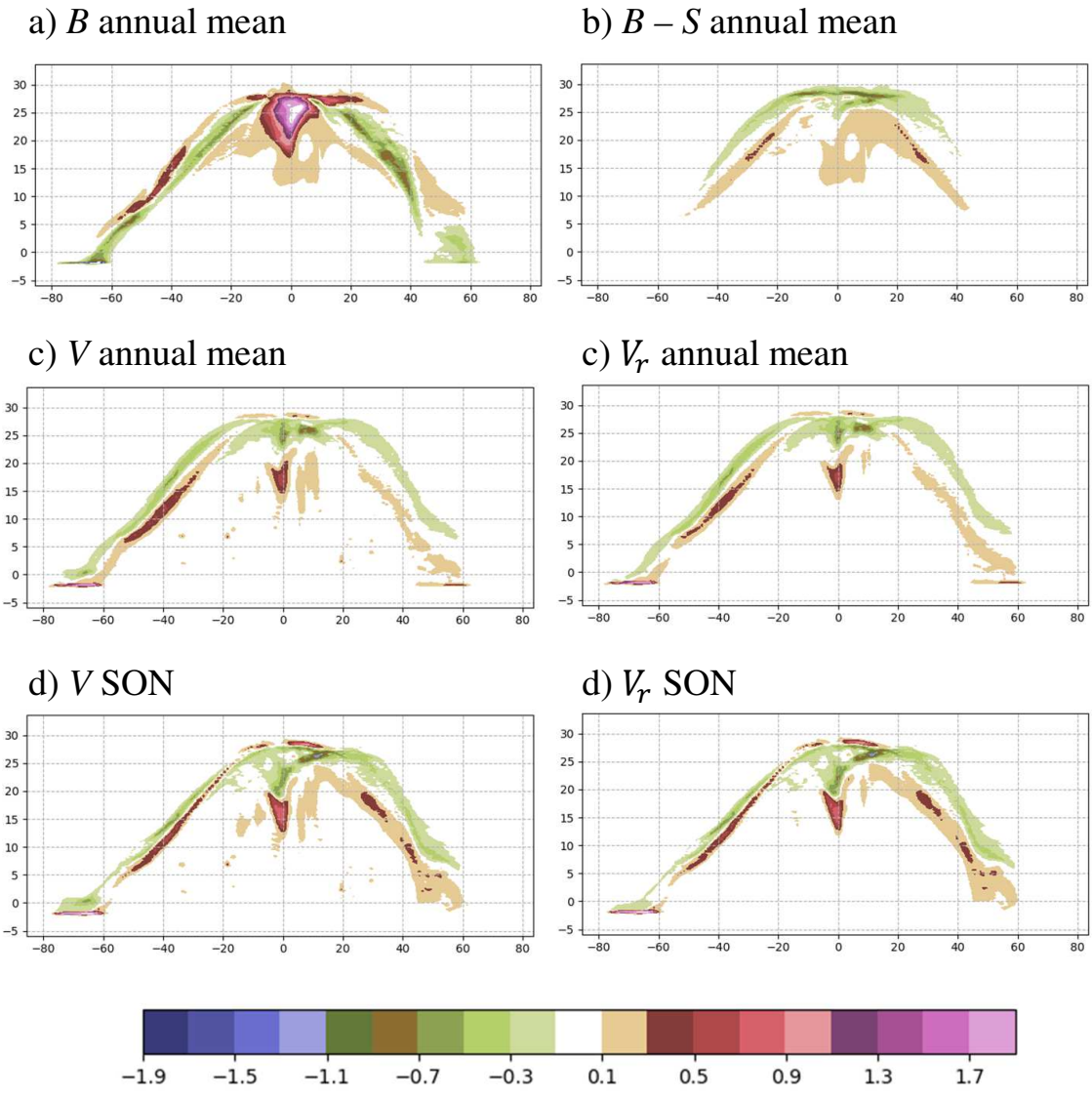

FIG. 6. Mean net heat flux divergences (10^{13}WK^{-1} per degree latitude) as a function of latitude (abscissa) and potential temperature class (ordinate) for the Pacific ocean from the LL control integration for the period 2000-2009. (a) Annual mean absorption of surface fluxes, B; (b) Difference between annual mean solar absorption at the true depth and the surface $B-S$; (c) and (e) Vertical diffusion, V; and (d) and (f) Vertical diffusion, V_r, limited to 1.2 times the monthly maximum mixed layer depth or 100m of the surface. (c) and (d) are annual means; (e) and (f) are means for the boreal fall (SON). Saturated values are coloured white.

Griffies 2019) into (i) an outward flux of the same mass but with salinity equal to the surface salinity (converted to a volume flux for the Boussinesq NEMO model):

$$e_V = \rho_0^{-1}(e-p-r_I), \tag{5}$$

where $e-p-r_I$ is the usual upwards mass flux associated with evaporation minus precipitation minus river input, and (ii) a massless source of salt balanced by an outward flux of freshwater:

$$e_s = 0.001\, s(e-p-r_I). \tag{6}$$

This massless salt source recovers the "virtual" surface source used in rigid-lid models. It is area integrated over the surface grid-cell $ij1$ to give

$$B_{V_{ij1}} = e_1 e_2 e_s, \tag{7}$$

which has the correct units kg s^{-1} and may then be binned in salinity like the other terms to give the binned B_V field. Of course, for (3) (with $B = B_V$) to remain valid it is now necessary to subtract this B_V from the advection A; this physically represents that the advection term now "sees" a surface inflow of water with salinity s rather than FW (salinity zero).

We have also calculated the monthly mean potential density, ρ, thermal expansion coefficient, α, and saline contraction coefficient, β, at each grid point using the model's equation of state (EOS80) and θ and s with $z = 0$. Each of the monthly mean density terms, X_ρ, where X stands for one of the letters in table 1, are then calculated from the corresponding potential temperature terms, X_θ, and salinity terms, X_s, using

$$X_\rho = \rho_0(-\alpha X_\theta + \beta X_s). \tag{8}$$

These values have been assigned to 200 classes of width 0.1kg m^{-3}.

In Boussinesq water-mass transformation theory (e.g. Nurser et al. 1999; Groeskamp et al. 2019), the binned heat inputs are generally divided by the bin width to give volume fluxes across the isotherms, according to

$$F_X = \frac{X}{\rho_0 c_p \Delta\theta}. \tag{9}$$

Given that the heat inputs are binned also in latitude, (9) would give volume flux across the isotherm within the latitude bin. Here, however, we choose to simply bin the heat, salt and mass fluxes because we are concentrating on the heating and freshening processes.

We use two measures for how well one field F_i represents a second field G_i. The first is a normalised sum of squared differences

$$D = \sum_i \frac{(F_i - G_i)^2}{S(F)S(G)} \quad , \quad S(F) \equiv \sqrt{\sum_i F_i^2}. \tag{10}$$

The smaller the value of D the better F reproduces G. The second measure is the correlation coefficient:

$$C = \sum_i \frac{F_i . G_i}{S(F)S(G)}. \tag{11}$$

b. How much of the vertical mixing is confined to near surface layers?

Figure 6 presents terms for the rate of change of heat content in the Pacific ocean. Panel (a) shows the annual mean Absorption term, B, which is the net of the heat input by solar radiation, taking account of the depth of penetration, and the heat lost from the surface due to turbulent fluxes and long-wave radiation. Panel (b) shows the annual mean $B - S$ where S is the net heat input taking all the solar radiation to be absorbed at the surface. One sees that the penetration of the solar flux makes an appreciable difference to the temperature distribution of the "surface" fluxes as noted in the introduction.

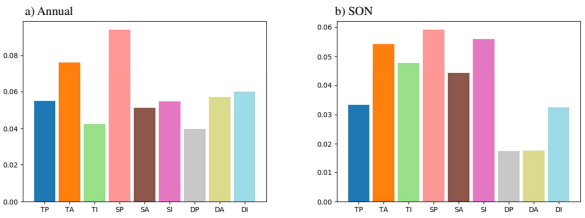

FIG. 7. The normalised mean square error in representing V by V_r calculated using (12) with $F = 1.2$ and $d_0 = 100$m for (a) annual means and (b) boreal fall (SON). The first letter, T, S or D, on the abscissa indicates potential Temperature, Salinity or Density respectively. The second leter, P, A or I, indicates the Pacific, Atlantic or Indian Ocean basin respectively.

The re-distribution of heat by Vertical diffusion, V, in the annual mean, shown in panel (c), also makes an appreciable difference to the temperature distribution of the surface fluxes. This re-distribution has a very strong seasonal variation, except possibly near the equator, with V being strongest in mid-latitudes during summer months (not shown). The large seasonal variation suggests that the dominant contribution to the Vertical diffusion may be associated with mixing within or just below the surface mixed layer. We have explored this hypothesis by calculating additional diagnostics, V_r, in the same way as V except that the contributions are restricted to depths less than d_{max} where

$$d_{\max} = \max\left(F \ . \ \mathrm{MLD}_{\max}, d_0\right). \tag{12}$$

Here $\mathrm{MLD}_{\max}$ is the maximum mixed layer depth in the month (as a function of geographical location) calculated following Kara et al. (2000), F is a factor slightly larger than 1 and d_0 is a constant value. One would expect a value of F of order 1.2 to be sufficient to capture vertical mixing confined to the mixed layer and entrainment into it. Comparison of V_r calculated using $F = 1.5$ and $d_0 = 0$ with the full V (not shown) reveals that not all of the vertical mixing is associated with mixed layer processes. Figure 6 displays V (left) and V_r (right) calculated using $F = 1.2$ and $d_0 = 100$m with annual mean and boreal fall data (in the middle and lower panels respectively). One sees that in both cases V_r using this combination reproduces V very closely. We conclude that although not all the vertical diffusion is associated with mixed layer processes, the vast majority of it is either associated with mixed layer processes or occurs within 100m of the surface.

Figure 7 shows that this result holds in the other ocean basins and for salinity and density as well as heat content. It displays the normalised sum of squared differences, (10),

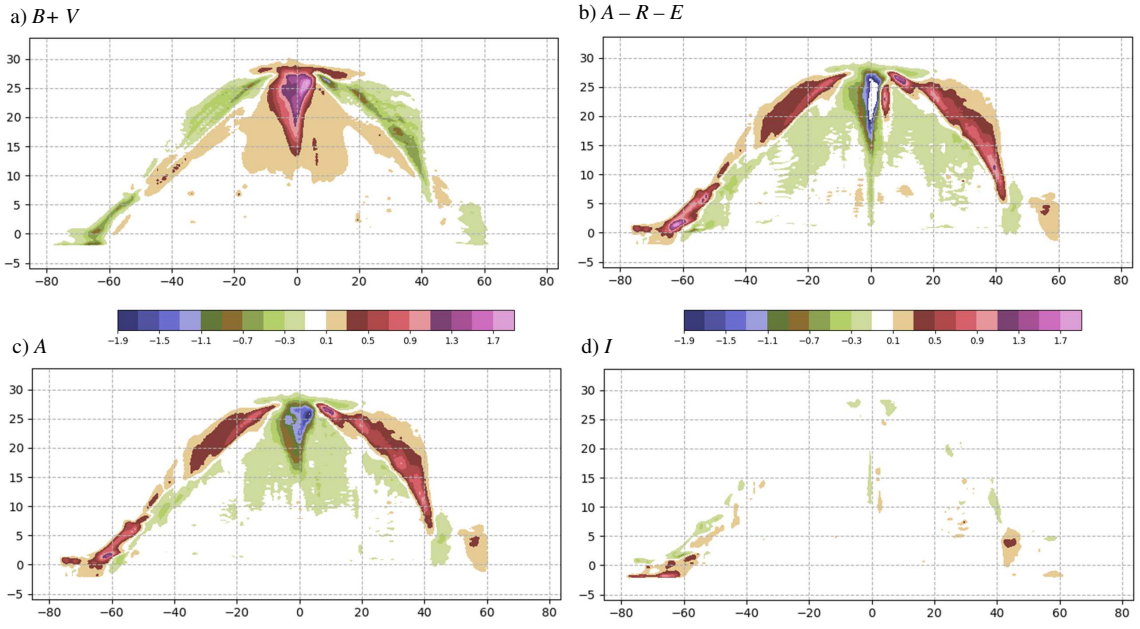

FIG. 8. As for figure 6 except that: (a) is Absorption plus Vertical Diffusion, $B+V$, (b) is the Mean Advection, $M = A-R-E$, (c) is total Advection, A, and (d) is Isopycnal diffusion, I.

between V_r and V calculated for each of these terms (a) using all months and (b) using the boreal fall months (SON). Similarly small values of D are obtained for the three other seasons.

c. *How well correlated are mean advection and near surface flux inputs?*

This subsection compares contributions from various estimates of the Advection and Isopycnal diffusion terms with $B+V$, the NSHF taking into account "near surface" vertical mixing. Our focus will be on the patterns in (ϕ, class) space of the advection by the mean flow, M (see (4)), because the interpretation of the previous section assumes that these terms are dominant, in which case they should be strongly anti-correlated with $B+V$. The total rate of change, T, is small (it would appear almost completely white using the contour intervals in figure 6). Using (3), this implies that many combinations of terms (such as $A+B$ and $I+V$) are almost perfectly anti-correlated for all of the tracers.

Starting with heat term contributions, Figure 8 allows one to compare $B+V$ for the LL Pacific simulation with $M = A-R-E$, A and I. It is clear that $B+V$ is very well anti-correlated with A. At high latitudes, particularly in the southern hemisphere, I makes an appreciable but by no means dominant contribution (Gregory 2000). One can see from panels (a), (c) and (d) that the regions at high latitudes where A and $B+V$ are not well anti-correlated are precisely those where I is non negligible.

In addition to the regions of strong negative values (representing cooling of water) at the equator, M and A in figure 8 have slanting regions of strong positive values (warming of water) which extend from close to the equator to about 40°N and 35°S. We interpret these as being associated with boundary currents advecting warm water poleward. It is evident from figures for R and E for the LL Pacific simulation (not shown) that the contributions from R are quite important near the equator and small elsewhere, whilst E makes its contributions at high latitudes, particularly in the southern hemisphere, and mid-latitudes. Like $B+V$, R warms the water on the equator. It seems very likely that this is associated with tropical instability waves fluxing heat towards the equator (e.g. Bryden and Brady 1989; Graham 2014). The fact that M is "balanced" by both B and $R+E$ on the equator is consistent with the idea that wind-driven Ekman upwelling is driving the uptake of heat from the atmosphere in this region.

Figure 9 presents $B+V$ and M from the LL integration calculated for the Atlantic ocean (top) and the Indian ocean (bottom). $B+V$ and M are clearly well anti-correlated in many regions of significant heat gain or loss. The heating by M in the Atlantic clearly extends much further north (as far as 80°) in the Atlantic than it does in the Pacific (only to 40°N). In the Indian Ocean, relatively little heat is absorbed at the equator and there are two distinct regions where heat is supplied by M and lost through surface fluxes $B+V$.

Figure 10 presents $R+E$ and I for the Atlantic from the LL and MM integrations. I is non-negligible over a

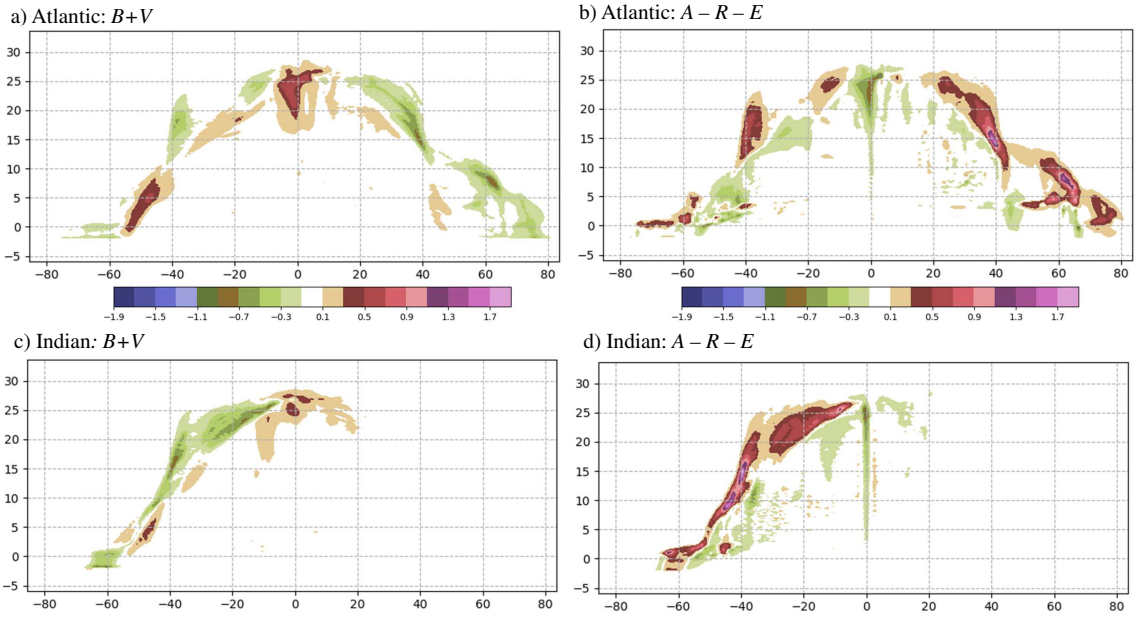

FIG. 9. As for figure 6(a) except the terms Absorption plus Vertical Diffusion, $B+V$, (left) and Mean Advection, $M=A-R-E$, (right) are presented for the Atlantic (top) and Indian oceans (bottom).

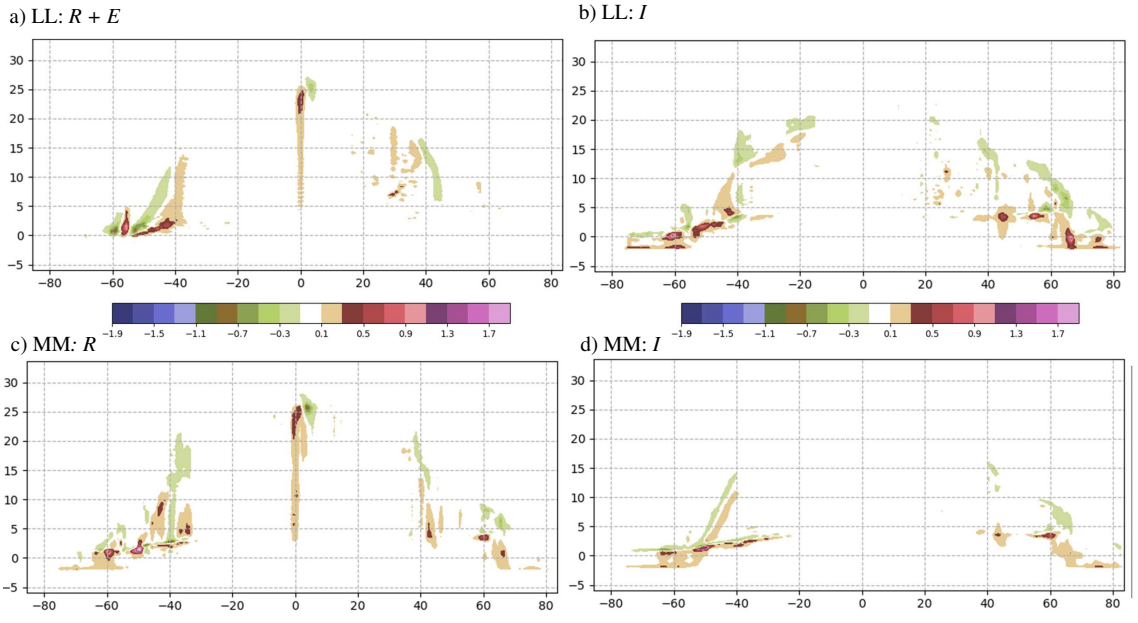

FIG. 10. As for figure 6(a) except that the terms are the sum of the Residual and Eddy-induced advections, $(R+E$, left) and the Isopycnal diffusion (I, right) calculated for the Atlantic Ocean from the LL (top) and MM (bottom) integrations.

wider region in the Atlantic than the Pacific particularly in the northern hemisphere. The factor of 6 reduction in the isopycnal diffusion coefficient in MM weakens I significantly but by a much smaller factor than 6 (fig 10 panels (b) and (d)). Despite setting $E=0$ in the MM integration, $R+E$ is of comparable importance in the LL and MM integrations, though away from the equator the patterns of the fields differ considerably.

In salinity space, (ϕ,s), the A, B_V, I and V terms are all of a similar order of magnitude. R is relatively small except close to the equator and, as mentioned already, E is unacceptably noisy at some points in (ϕ,s) space. As it is relatively small compared to the other main terms at other

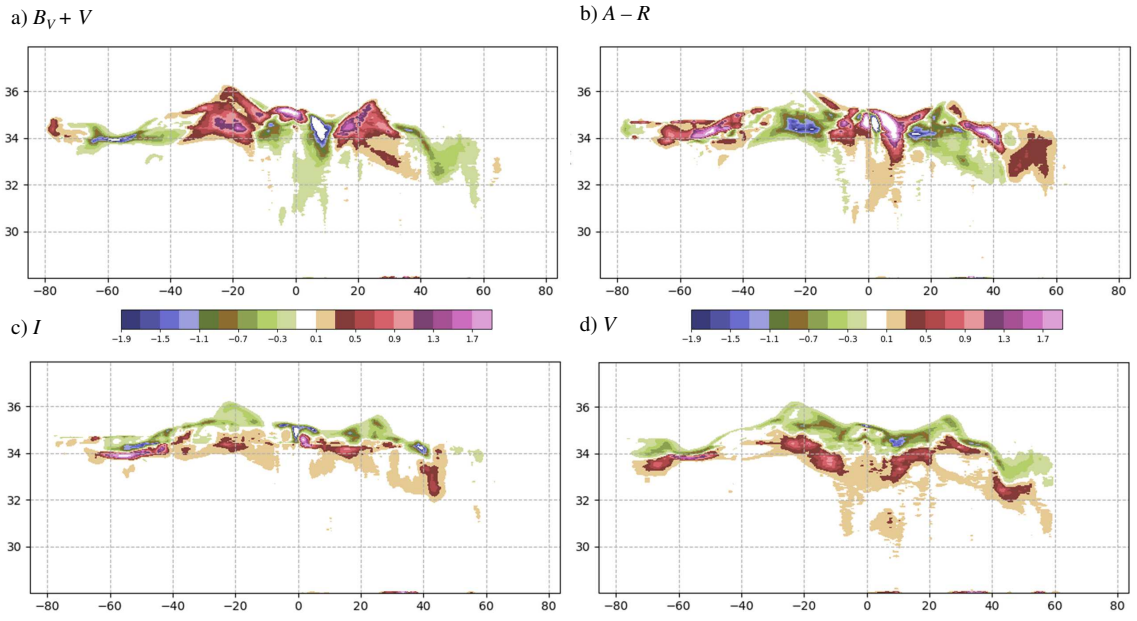

FIG. 11. Annual mean net salt flux divergences (10^6kgs^{-1}psu^{-1} per degree latitude) as a function of latitude (abscissa) and salinity class (ordinate) for the Pacific ocean from the LL control integration for the period 2000-2009. (a) Virtual salt flux plus vertical diffusion, $B_V + V$, (b) Mean advection, $M = A - R$, (c) Isopyncal diffusion, I, and (d) Vertical diffusion, V.

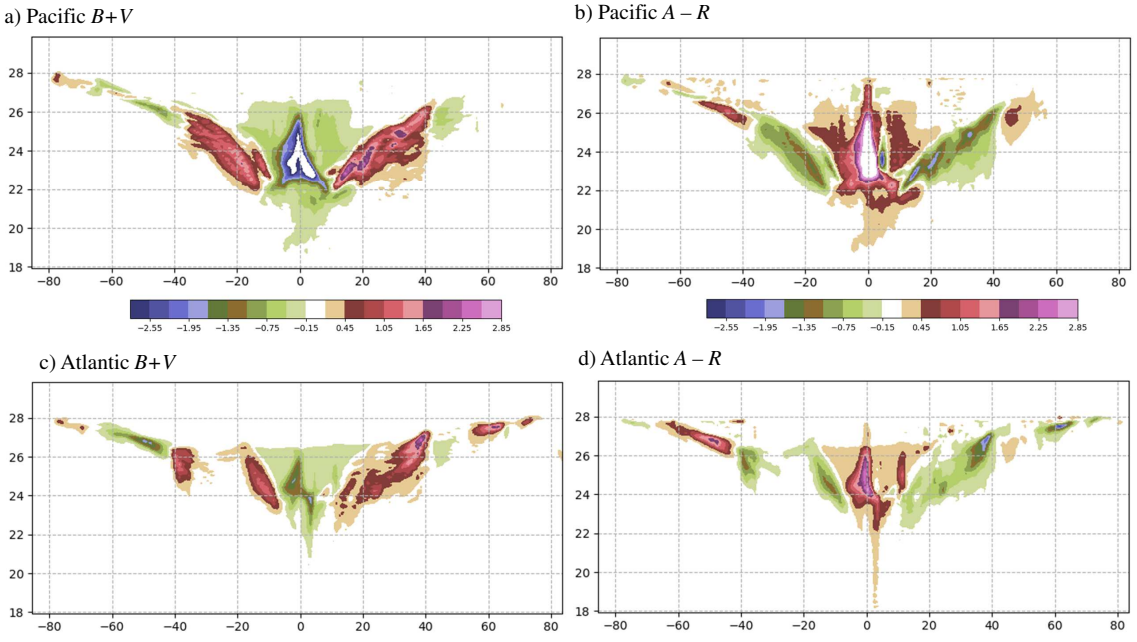

FIG. 12. As for figure 6(a) except that potential density terms in (ϕ, ρ) space, with units 10^6m^{3}s^{-1} per degree latitude, are presented for Absorption plus Vertical Diffusion, $B + V$, (top) and Mean advection, $A - R$, (bottom) in the Pacific (left) and Atlantic (right) Oceans.

points in (ϕ, s) space, we estimate M for salinity from $A - R$ neglecting E. Figure 11 compares $B + V$, $A - R$, I and V for the Pacific. Even though I is relatively more important than before, $B + V$ and $A - R$ are clearly anti-correlated. In all three ocean basins, positive values of B_V generally occur for higher salinites than the negative values and the opposite is true for I and V (not shown). A similar pattern is much less marked in $B + V$ and is not discernible in M.

In potential density space, (ϕ, ρ), the isopycnal diffusion term I is small (it is not exactly zero for several reasons).

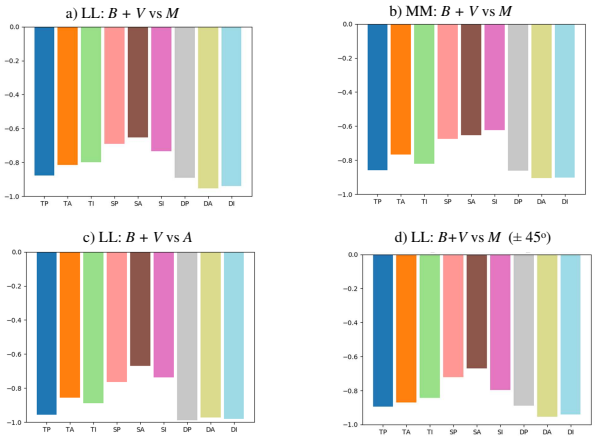

FIG. 13. The pattern correlation coefficients in (ϕ, class) space calculated using (11) for the terms $B+V$ and M for (a) the LL and (b) the MM integrations. Pattern correlations as in (a) but (c) for the terms $B+V$ and A and (d) restricting the latitudes to within 45° of the equator. The first letter, T, S or D, on the abscissa indicates the class: potential Temperature, Salinity or Density respectively. The second letter, P, A or I, indicates the Pacific, Atlantic or Indian ocean basins respectively.

So $B+V$ and A are very strongly anti-correlated, and $B+V$ and $A-R$ are more strongly anti-correlated than they are for θ. Figure 12 presents the patterns of $B+V$ and $A-R$ in the Pacific and Atlantic Oceans for the LL integrations. Potential density varies much more slowly with θ in cold water than warm water so the arms of the horse-shoe shape in the upper panels of figures 8 and 9 are compressed in figure 12 as well as inverted (because density decreases as temperature increases). As anticipated, in both basins the patterns in $B+V$ are well anti-correlated with those of $A-R$.

Panels (a) and (b) of figure 13 provide a convenient summary of the pattern correlations in (ϕ, class) space calculated using (11) between $B+V$ and M for each of the three classes and three main basins in the LL and MM integrations; for salinity and density M is calculated from $A-R$ whilst for heat it is calculated from $A-R-E$. The magnitude of the correlations is clearly largest for ρ (> 0.85), smallest for s (between 0.6 and 0.7) and between 0.75 and 0.85 for θ. It varies somewhat depending on the ocean basin and the model resolution. Comparison of panels (c) and (a) shows that the magnitude of the correlation between $B+V$ and A is slightly greater than that between $B+V$ and M for s and θ and considerably greater for ρ. Comparison of panels (d) and (a) shows that the magnitudes of the correlations between $B+V$ and M for θ are somewhat increased when the region considered is restricted to that within 45° of the equator.

d. How much spurious mixing is produced by advection?

In a Boussinesq rigid-lid model (e.g. Gordon et al. 2000, Gregory 2000) the integral, $I_A(\tau_0)$, of the divergence of the advective flux of any tracer, τ, over a volume V_0 where $\tau(x,y,z) > \tau_0$ that is bounded by the part of the air-sea interface where $\tau > \tau_0$, land boundaries and the isopleth $\tau = \tau_0$, should be zero. This result is derived in two steps. First, a rigid-lid model requires there to be no flow across the air-sea interface, so I_A depends only on the flux across the isopleth:

$$I_A(\tau_0) \equiv -\int_{V_0} \nabla.(\tau \mathbf{u}) \mathrm{d}V = -\tau_0 \int_{\partial V_{0\tau_0}} \mathbf{u}.\hat{\mathbf{n}} \mathrm{d}S, \qquad (13)$$

$\partial V_{0\tau_0}$ denoting the boundary where $\tau = \tau_0$. Second, by the Boussinesq assumption the flow is incompressible within V_0, and since there is no volume flow across the surface or land boundaries there can be none across the isopleth $\partial V_{0\tau_0}$. So the final term on the rhs of (13) is zero, and $I_A(\tau_0) = 0$.

In such a model, any deviations of $I_A(\tau_0)$ from zero can be ascribed to numerical mixing: i.e. different choices of τ in calculating the model advective flux at different cell faces making up the discrete representation of $\partial V_{0\tau_0}$.

However, modern ocean models such as the NEMO v3.6 configuration diagnosed here allow a fully non-linear free surface in which mass flux is permitted across the air-sea interface (see (5)), and the cell thicknesses vary as the free surface height changes. In such models $I_A(\tau_0) \neq 0$, even without numerical mixing. We show in the Appendix that for our model

$$I_A(\theta_0) = \theta_0 \left[\int_{\partial V_{0s}} e_V \mathrm{d}S + \int_{V_0} \frac{1}{e_3} \frac{\partial e_3}{\partial t} \mathrm{d}V \right], \qquad (14)$$

$$I_A(s_0) = \int_{\partial V_{0s}} e_V (s_0 - s) \mathrm{d}S + s_0 \int_{V_0} \frac{1}{e_3} \frac{\partial e_3}{\partial t} \mathrm{d}V, \qquad (15)$$

∂V_{0s} denoting the boundary of V_0 at the air-sea interface. The expected value of A for the heat budget is $c_p \rho_0 I_A(\theta_0)$ whilst that for the salt budget is $0.001\, \rho_0\, I_A(s_0)$.

The different forms of (14) and (15) arise from the fact that the heat content of the water passing through the surface is considered as part of the absorption (B) term for heat, but the salt content of the water passing through the surface associated with the mass flux e_v in (5) is assigned to the residual advection (A) after the the virtual salt flux B_V has been split out from the original advection term.

Our discussion follows Holmes et al. (2019a) and Holmes et al. (2021) who use similar integrals to provide insights into the potential weaknesses of their model configurations but is limited by the fact that we have only been able to assign accumulated terms from the tracer equations to tracer classes using monthly mean tracer values. The integrals for the total advection term will contain errors

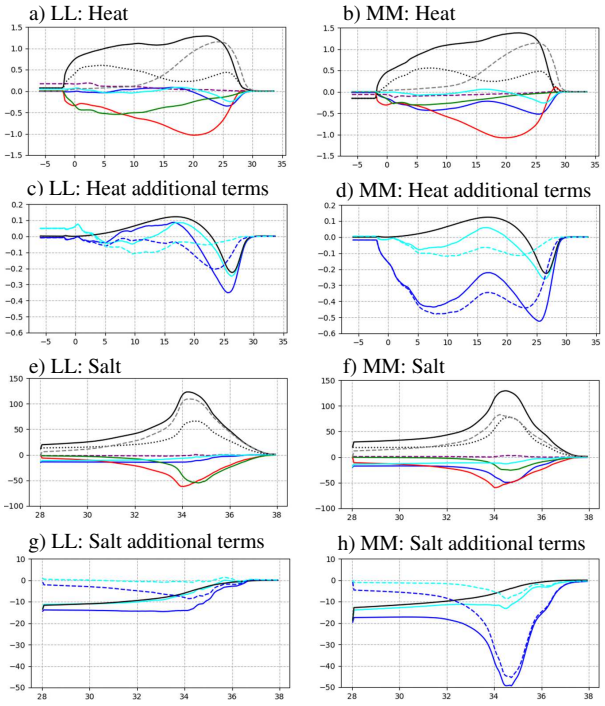

FIG. 14. (a) and (b): Integrals of heat content tendency terms (ordinate with units of PW) over all points in the global domain where $\theta > \theta_0$, θ_0 is the abscissa. The terms and their line colours are: Advection,A, blue; Absorption, B, black; Isopyncal diffusion, I, green; Mean advection, M, cyan; Vertical diffusion, V, red; $B+V$ black dotted; $S-B$ grey dashed. (a) and (b) are results for the LL and MM control integrations respectively. (c) and (d): As for (a) and (b) except that the terms, lines and colours are: the expected value for A, calculated using (14), black; Advection, A, full blue; A minus its expected value, dashed blue; Mean Advection, M, full cyan; M minus its expected value, dashed cyan. (e) and (f): As for (a) and (b) except that the integrals are of the salt content tendencies (with units psu Sv) as a function of salinity and the grey dashed line is $A+B_V$. (g) and (h): As for (e) and (f) but the terms, lines and colours are: the expected value for A calculated using (15), black; Advection, A, full blue; A minus its expected value, dashed blue; Mean original Advection M, full cyan; M minus its expected value, dashed cyan.

because of this, but the advection by the monthly mean flow of the monthly mean tracer field should satisfy (14) or (15).

Panels (a)–(d) of Figure 14 present the integrals, over all the points in the global domain where $\theta > \theta_0$, of a number of heat content tendency terms from the LL (left) and MM (right) integrations. Panel (a) shows that in the LL integration there is a net global Absorption, B, of heat of about 1.3PW (full black line) for $\theta_0 > 23°$C and that about two thirds of this heat is lost in waters with $\theta_0 < 0°$C. Vertical diffusion, V, (red line) re-distributes this heat, offsetting the input by B, so that their sum, $B+V$, (dotted black line) is relatively modest, compared to B, for $\theta_0 > 15°$C. The difference in heat input due to the penetration of solar radiation, $S-B$, (grey dashed line) is substantial for $\theta_0 > 15°$C. Were all solar radiation absorbed at the surface, the net heat input would be the sum of B and $S-B$ and exceed 2.2PW for $\theta_0 > 25°$C. Isopycnal diffusion, I (green line), and Advection, A (blue line), together oppose $B+V$. The total tendency, T (purple dashed line) is fairly close to zero but has a noticeable input of heat at around $\theta_0 = 4°$C and a global net imbalance of about 0.15PW.

Advection and the Mean advection, $A-R-E$ (full cyan line), are non-zero, the peak discrepancy occuring just above 25°C. The black line in panel (c) is the expected value for the advection term, $c_p\rho_0 I_A(\theta_0)$, calculated using (14) . The dashed lines in panel (c) are the integrals of A (blue) and $A-R-E$ (cyan) with this expected value subtracted. One sees that the error in $A-R-E$ is quite small and that the error in A is smaller than one would infer if (14) is not taken into account. Panels (b) and (d) of Figure 14 show the corresponding results for the MM integration. One sees that the I term is reduced by about a half (its coefficients have been reduced by a factor of six) and A is significantly larger than in the LL integration, though as mentioned earlier our calculation does not allow us to firmly conclude that this is due to spurious advection. Panel (d) also shows that the error in M (dashed cyan) is still small.

Panels (e) to (h) present the corresponding results to panels (a) to (d) for contributions to the rate of change of salt content by salinity class. The line colours and styles in panels (e) and (f) match those in panels (a) and (b) except that the grey dashed lines in panels (e) and (f) are the sum of the Advection and Absorption terms, $A+B_V$. Noting that T (purple dashed line) is small, (3) implies that $A+B_V$ must be almost equal and opposite to $I+V$. Diffusion terms are expected to flux salt from smaller and larger values towards intermediate values. So their integrals in Figure 14 are expected to have negative values consistent with both the I (green) and V (red) lines. In both panels (g) and (h), the expected value for the integral of A (black line) agrees well with the integral of the Mean advection term ($A-R$, solid cyan). Its agreement with the integral of the Advection term (A, solid blue) is good in the LL integration and significantly less good in the MM integration, leaving an appreciable difference between them (blue dashed line).

e. What are the main sources of the heat lost in the north Atlantic?

Figure 3 presents the sums over all classes of the net heat and salinity flux divergences by Advection (A) and Surface fluxes (S) for a number of latitude bands in each ocean basin. To within machine precision, V and $B-S$ are zero for these quantities, so the values for S are the same as those for B and $B+V$. Comparison of panels (b) and (e) and of (c) and (f) shows that the B and A heat fluxes are almost equal and opposite in the LL and MM integrations respectively. Panels (e) and (f) show that the

latitude band sums of A are also rather similar in the LL and MM integrations, the most notable differences being in the Indian Ocean. In the Indian Ocean, it is clear that in the LL integration more heat is lost to the atmosphere (between 45°S and 15°S) than is gained (between 15°S and 15°N). This is much less pronounced in the MM integration. The dominance of the equatorial Pacific regions in the 2.3PW of annual mean ocean heat uptake (Forget and Ferreira 2019) is particularly marked in the LL integration (panel b). The latitude band sums of $A-R-E$ (not shown) and A are rather similar. Panel (g) (whose ordinate has been rescaled) shows that $R+E$ cools the equatorial belt and that its latitude band sums, like those of I (not shown), are about a factor of 10 smaller than those of A and B. These sums of I and $R+E$ have a tendency to cancel each other particularly south of 30°S.

Panels (h) and (i) of figure 3 show corresponding results to (e) and (b) for the A and B saline flux divergences. Precipitation, evaporation and river inflow make the subtropical gyres (between 15° and 30° in both the southern and northern hemispheres) more salty and the equatorial and high latitudes less salty. A and $-B$ are again very similar, the largest differences being in the 60°S to 45°S band. A in the MM integration (not shown) is also similar to the LL integration, the largest differences being in the Atlantic in the equatorial and 60°S to 45°S bands.

Returning to panel (c) one sees that the heat lost in the Atlantic north of 60°N is much greater than the heat input into the Atlantic and Indian Oceans between 60°S and 45°S. This is contrary to what the schematic view presented in Figure 4 suggests but potentially consistent with the analysis of Talley (2013), Forget and Ferreira (2019) and Holmes et al. (2019b). Figure 15 allows this issue to be investigated in some detail. It shows the heat input (in 10^{14} Watts per Kelvin) by $B+V$ (red solid), A (green solid), and $A-R-E$ (blue dashed) for each basin and selected latitude bands. We have seen (panel (c) of Figure 14) that the global error in $A-R-E$ is relatively small and one can see from panel (c) of Figure 15 that except for water colder than about 2°C the regional and global values of $B+V$ and $A-R-E$ as a function of θ are approximately equal and opposite. One can consider for a given θ which regions take up the heat lost in other regions. None of the regions has a net loss of heat ($B+V$ term) with $\theta > 26$°C, and there is a global net heat input for $\theta > 26$°C clearly apparent in panel (c). The heat lost between 20°C and 25°C in the north Atlantic and the southern and equatorial Indian Ocean is mainly compensated by heat taken up in the equatorial Pacific and equatorial Atlantic but there is a small heat loss globally at these potential temperatures. Panel (b) shows that the north Atlantic loses about 0.03PWK^{-1} of heat fairly uniformly for θ between 0°C and 20°C. Panels (j) - (l) show that the Pacific is the only ocean that has a net uptake of heat for θ between 8°C and 20°C. Panel (c) shows that this uptake of heat in the Pacific exceeds the heat loss in the Atlantic and Indian oceans. Panels (d) and (e) respectively show that the range of θ warmed in the equatorial Pacific extends down as far as 5°C, and that it only extends down to about 13°C in the equatorial Atlantic. The southern Pacific, Atlantic and Indian Oceans take up heat for θ between 8°C and 13°C, 0°C and 10°C and 2°C and 8°C respectively. This uptake of heat must be obscured in panel (c) of figure 3 by heat loss in other θ ranges.

In conclusion, the differences between the heat uptake in the equatorial Pacific, Atlantic and Indian oceans, evident in figure 15 panels (d) - (f), are as remarkable as the more well known differences between the heat lost in the north Atlantic and Pacific oceans, panels (a) and (b). The net heat uptake by the Pacific, panel (j), plays a major role in feeding the heat lost over a wide range of potential temperatures in the Indian and Atlantic oceans, panels (k) and (l), and the heat uptake in the equatorial Pacific, panel (c), makes a significant contribution to the heat lost in the north Atlantic, panel (b).

4. Concluding summary and discussion

The decadal mean NSHF for 2000-2009 from the low resolution HadGEM3-GC3.1 historical integration has been shown (figure 1) to agree well with the DEEPC reanalysis products based on ERA-interim data for the same period. The NSHFs for this coupled climate model are also relatively insensitive to resolution (see figure 2), the main differences being in the north Atlantic and Agulhas retroflection regions where the NSHFs from the higher resolution simulations agree better with the DEEPC reanalyses. We have taken this opportunity to outline a relatively simple dynamical interpretation of the geographical patterns of the NSHFs visible in figure 1 in which cooling of the near surface by wind-driven upwelling, the influence of boundary waves in reducing along-boundary density gradients, and heat input to higher latitudes from poleward advection by the time-mean flow all play prominent roles.

As a step in the investigation of the validity and limitations of this interpretation, we have examined the main terms (see table 1) in the time-mean tracer budgets in this climate model for potential temperature, salinity and potential density in the main ocean basins. We have shown that nearly all the contributions from vertical mixing occur either within 100m of the surface or within 1.2 times the monthly maximum mixed layer depth (figure 6). Plotting the heat budget terms as a function of latitude and potential temperature, we have also shown that the sum of the absorption of the surface heat flux and vertical mixing terms (B and V respectively) is well anti-correlated with the total advection (A) and with the time-mean advection (M) in each of the basins. This supports the hypothesis that, over much of the ocean, time-mean advection is the dominant process (locally) in balancing the heat input and stirred by

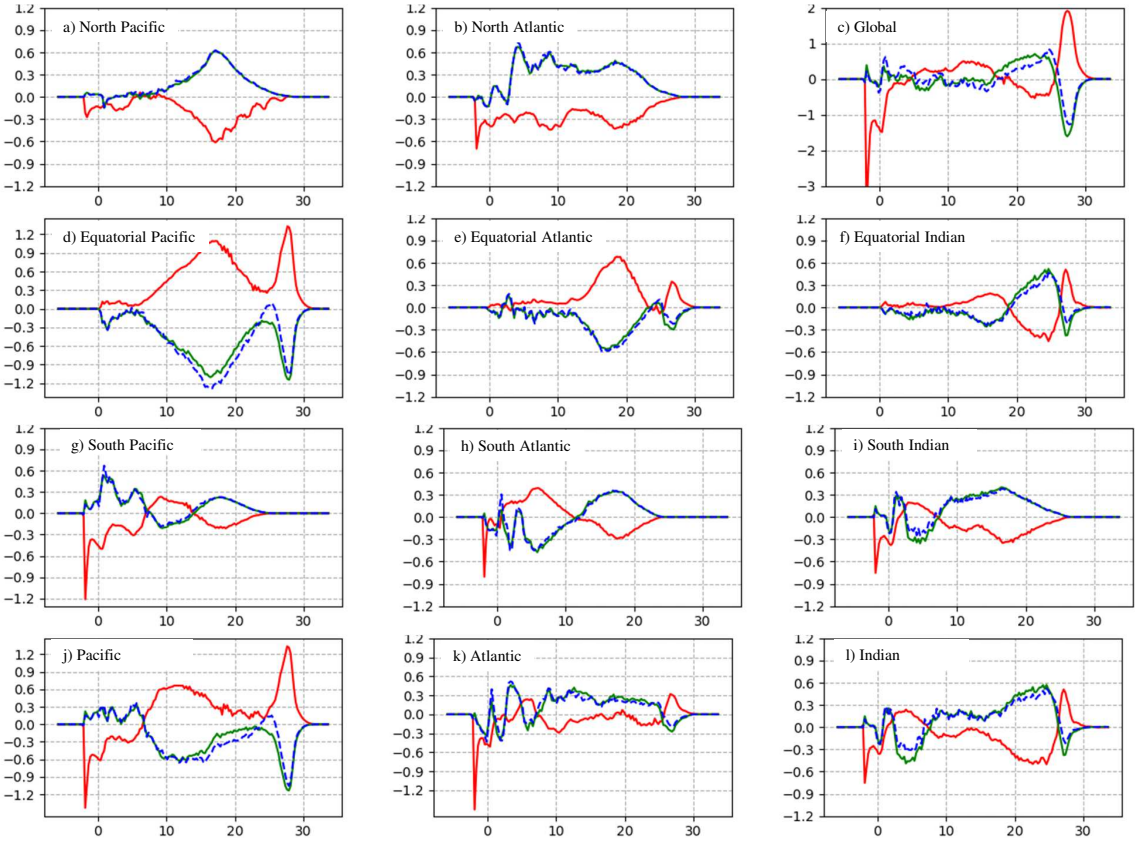

FIG. 15. Net heat input (units 10^{14} Watts per Kelvin) as a function of θ by $B+V$ (red solid), A (green solid), and $A-R-E$ (blue dashed) for selected basins and latitude bands.

the air-sea fluxes of heat and momentum. This interpretation follows the spirit of the surface streamfunction concept (Marsh 2000) whilst recognising that the modification of the surface heat fluxes by the penetration of solar radiation and vertical mixing is very significant. The anti-correlation of $B+V$ and M is stronger for potential density and weaker for salinity than it is for potential temperature (see figure 13) suggesting that a similar interpretation applies well for potential density and is much less satisfactory for salinity.

We have also shown that the simple schematic of figure 4 does not capture the main terms in the heat budget in some geographical regions. At high latitudes in the Southern Ocean and the north Atlantic, isopycnal diffusion and/or transports by the time-varying flow are significant. These limitations are consistent with expectations based on Gregory (2000) and Munday et al. (2013). Very close to the equator, transports by the time-varying flow, R, (e.g. by tropical instability waves) significantly reduce the cooling by advection.

Furthermore we have shown that the net heat input by latitude bands (summed over all potential temperature classes), which is identically zero for purely vertical mixing, is dominated by a balance between the NSHF and the advection (see figure 3). The net heat input by potential temperature class (summed over all latitudes) should be close to zero (Walin 1982). We have calculated a residual value (14) that arises from fluxes of water across the air-sea interface and shown that this correction should not be neglected (Figure 14). We have also argued that the heat taken up in the equatorial Pacific makes a significant contribution to the heat lost in the north Atlantic (Figure 15) supporting the analysis of Talley (2013), Forget and Ferreira (2019) and Holmes et al. (2019b).

We have argued that tracer advection is very important in the heat budget and MOCs, despite the restrictions on it imposed by the mathematical fact that, in a seasonally varying equilibrium, it must be very close to zero in global integrals over tracer classes. McWilliams et al. (1996) examined the conundrum that arises if one supposes that the diapycnal mixing across a low latitude "warm water" volume bounded by an isotherm, such as the 20°C isotherm, could not be strong enough to balance the NSHF input. They found that the diapycnal mixing in their (coarse resolution) model did balance the NSHF. It may be helpful to consider this issue from the perspective in which it is assumed that surface fluxes, vertical mixing and advection

are the only processes involved in the heat budget. Cold water driven to the surface near the equator by the winds is only warmed when it reaches the region where there is surface heat input or vertical mixing of that heat input. In the absence of the NSHF, the water advected away to other latitudes would have the same temperature as it did when it was advected into the region, and there would be no net advective heat input. Similarly, as the water near the surface is advected to higher latitudes, it will only change its temperature when it is cooled by the NSHF (or water from below is mixed vertically into it). In this sense the advective term in the heat budget is totally dependent on the NSHF (and mixing processes). If one considers only the heat budget, its terms appear to have a curiously elusive, "chicken and egg", nature. This argument is also relevant to the assessment of the importance of the parametrisation of the solar penetration. One might be tempted to conclude from figure 6 that this is very important for the heat budget and that its dependence on the water clarity and ocean biology must also be very important (Murtugudde et al. 2002). Changes to the penetration of solar radiation can give large local changes in the differences between the model and observations but their impacts on the heat budget in potential temperature space would be more subtle.

One of the limitations of our study is that we have not accumulated terms by tracer class "on the fly" at every time-step. That would enable better calculation of global budgets by tracer class. We believe that it would be possible to implement this in a modular and sustainable manner. The accumulation of these diagnostics would require the relevant decades of the model integration to be repeated and would increase the size of the diagnostic outputs as the data would be saved as 3D fields. "On the fly" accumulation of vertical mixing contributions within and just outside the surface mixed layer would also need to be carefully considered. We have also not explored in detail the differences between the DEEPC and coupled model fluxes (figure 2) near the equator. One might investigate whether advection driven by Ekman upwelling or other processes is able to support as broad a region of ocean heat input near the equator as the DEEPC products. The net heat input into the ocean between 15°S and 15°N is also clearly larger in the DEEPC products than the coupled model.

This paper has only touched on one aspect of the interpretation of coupled model simulations in the light of conceptual models of meridional overturning circulations. Other investigations that would complement this study include ones on: variations in the depths of isopycnals along the eastern (and western) boundaries of the major ocean basins; relationships between zonal-mean wind stresses and NSHFs in the equatorial regions; and relationships between isothermal and isopycnal depths on eastern boundaries and heat fluxes into northern basins. Although the relationships between net surface fluxes and MOCs in coupled "control" integrations is of interest in its own right, the primary aim of our studies is to develop diagnostics that provide useful insights into simulations of climate change.

Acknowledgments. Bell and Storkey were supported by the Met Office Hadley Centre Climate Programme funded by BEIS. Nurser acknowledges support from the NERC project CLASS (NE/R015953/1). The authors gratefully acknowledge contributions from Pat Hyder and suggestions from David Marshall.

Data availability statement. The authors will make the code and input data used to generate the figures available from a github repository once the paper has been accepted.

APPENDIX

Calculation of the integral of the advection term over a domain bounded by a tracer isopleth

We start our derivations of (14) and (15) from the tracer advection equation obtained from (1) and (2) by setting $V_{ijk} = I_{ijk} = B_{ijk} = 0$, dividing by $e_1e_2e_3$ and recognising that e_1 and e_2 are independent of k and t:

$$\frac{1}{e_1e_2e_3}\left(\frac{\partial(e_2e_3u\tau)}{\partial i}+\frac{\partial(e_1e_3v\tau)}{\partial j}+\frac{\partial(e_1e_2\omega\tau)}{\partial k}\right) = -\frac{1}{e_1e_2e_3}\frac{\partial(e_1e_2e_3\tau)}{\partial t} = -\frac{1}{e_3}\frac{\partial(e_3\tau)}{\partial t}. \tag{A1}$$

We note for use below that the model's continuity equation can be obtained by setting $\tau = 1$ in (A1), that the volume of a grid-cell element $\mathrm{d}V$ is indeed given by $\mathrm{d}V = e_1e_2e_3\mathrm{d}i\,\mathrm{d}j\,\mathrm{d}k$, and that the upward vertical velocity across the s-coordinate at the free surface, ω_s, is given by

$$\omega_s = e_V, \tag{A2}$$

where e_V is defined in (5).

Integrating (A1) over the volume V_0 used to define $I_A(\tau_0)$ in (13), using the divergence theorem and (A2) we obtain

$$I_A(\tau_0) = -\tau_0\int_{\partial V_{0\tau_0}}\mathbf{u}.\hat{\mathbf{n}}\mathrm{d}S - \int_{\partial V_{0s}}\tau_s e_V\mathrm{d}S. \tag{A3}$$

In our model the rate of change of heat content of the ocean associated with the water crossing the interface is treated as a surface flux. So $\tau_s = 0$ in the calculation of the tracer advection for both potential temperature and salinity, and the second of the two terms on the rhs of (A3) is zero. Using the continuity equation (i.e. (A1) with $\tau = 1$), integrating over the volume V_0, one can show that

$$-\int_{\partial V_{0\tau_0}}\mathbf{u}.\hat{\mathbf{n}}\mathrm{d}S = \int_{V_0}\frac{1}{e_3}\frac{\partial e_3}{\partial t}\mathrm{d}V + \int_{\partial V_{0s}}e_V\mathrm{d}S. \tag{A4}$$

Substituting (A4) in (A3) and setting $\tau = \theta$ one obtains (14). Subtracting the surface "virtual" salt flux, $1000B_V/\rho_0$, from (A3), setting $\tau = s$ and using (5) - (7) one obtains (15).

References

Adcroft, A., and J.-M. Campin, 2004: Rescaled height coordinates for accurate representation of free surface flows in ocean circulation models. *Ocean Modelling*, **7,3**, 269–284, https://doi.org/10.1016/j.ocemod.2003.09.003.

Bell, M. J., 2015a: Meridional overturning circulations driven by surface wind and buoyancy forcing. *J. Phys. Oceanogr.*, **45**, 2701–2714, doi: 10.1175/JPO–D–14–0255.1.

Bell, M. J., 2015b: Water mass transformations driven by Ekman upwelling and surface warming in sub-polar gyres. *J. Phys. Oceanogr.*, **45**, 2356–2380, doi: 10.1175/JPO–D–14–0251.1.

Broecker, W. S., 1991: The great ocean conveyor. *Oceanography*, **4,2**, 79–89.

Bryden, H. L., and E. C. Brady, 1989: Eddy momentum and heat fluxes and their effects on the circulation of the equatorial Pacific Ocean. *J. Mar. Res.*, **47**, 55–79.

Dias, F. B., C. M. Domingues, S. J. Marsland, S. M. Griffies, S. R. Rintoul, R. Matear, and R. Fiedler, 2020: On the superposition of mean advective and eddy-induced transports in global ocean heat and salt budgets. *J. Climate*, **33**, 1121–1140, https://doi.org/10.1175/JCLI-D-19-0418.1.

Exarchou, E., T. Kuhlbrodt, J. M. Gregory, and R. S. Smith, 2015: Ocean heat uptake processes: a model intercomparison. *J. Climate*, **28, 2**, 887–908, https://doi.org/10.1175/JCLI-D-14-00235.1.

Forget, G., and D. Ferreira, 2019: Global ocean heat transport dominated by heat export from the tropical Pacific. *Nature Geoscience*, **12**, 351–354, https://doi.org/10.1038/s41561-019-0333-7.

Fox-Kemper, B., and Coauthors, 2021: Ocean, cryosphere and sea level change. *Climate Change 2021: The Physical Science Basis. Contribution of Working Group I to the Sixth Assessment Report of the Intergovernmental Panel on Climate Change*, V. Masson-Delmotte, P. Zhai, A. Pirani, S. L. Connors, C. Pean, S. Berger, N. Caud, Y. Chen, L. Goldfarb, M. I. Gomis, M. Huang, K. Leitzell, E. Lonnoy, J. B. R. Matthews, T. K. Maycock, T. Waterfield, O. Yelekci, R. Yu, and B. Zhou, Eds., Cambridge University Press.

Gaspar, P., Y. Gregoris, and J.-M. Lefevre, 1990: A simple eddy kinetic energy model for simulations of the oceanic vertical mixing: Tests at station Papa and long-term upper ocean study site. *J. Geophys. Res.-Oceans*, **95**, 16 179–16 193, https://doi.org/10.1029/JC095iC09p16179.

Gent, P. R., and J. C. McWilliams, 1990: Isopycnal mixing in ocean circulation models. *J. Phys. Oceanogr.*, **20 (1)**, 150–155, https://doi.org/10.1175/1520-0485(1990)020<0150:IMIOCM>2.0.CO;2.

Gnandesikan, A., 1999: A simple predictive model of the structure of the oceanic pycnocline. *Science*, **283**, 2077–2081.

Gnandesikan, A., R. D. Slater, P. S. Swathi, and G. K. Vallis, 2005: The energetics of ocean heat transport. *J Climate*, **18**, 2604–2616, https://doi.org/10.1175/JCLI3436.1.

Good, S. A., M. J. Martn, and N. A. Rayner, 2013: EN4: quality controlled ocean temperature and salinity profiles and monthly objective analyses with uncertainty estimates. *J. Geophys. Res.-Oceans*, **118**, 6704–6716, https://doi.org/10.1002/2013JC009067.

Gordon, A. L., 1986: Interocean exchange of thermocline water. *Journal of Geophysical Research*, **91, C4**, 5037–5046.

Gordon, C., C. Cooper, C. A. Senior, H. Banks, J. M. Gregory, T. C. Johns, J. F. B. Mitchell, and R. A. Wood, 2000: The simulation of sst, sea ice extents and ocean heat transports in a version of the hadley centre coupled model without flux adjustments. *Climate Dynamics*, **16**, 147–168, https://doi.org/10.1007/s003820050010.

Graham, T., 2014: The importance of eddy permitting model resolution for simulation of the heat budget of tropical instability waves. *Ocean Modelling*, **79**, 21–32, https://doi.org/10.1016/j.ocemod.2014.04.005.

Gregory, J. M., 2000: Vertical heat transports in the ocean and their effect on time-dependent climate change. *Clim. Dyn.*, **16**, 501–515.

Gregory, J. M., and Coauthors, 2016: The Flux-Anomaly-Forced Model Intercomparison Project (FAFMIP) contribution to CMIP6: investigation of sea-level and ocean climate change in response to CO2 forcing. *Geosci. Model Dev.*, **9**, 3993–4017, https://doi.org/10.5194/gmd-9-3993-2016.

Griffies, S. M., and Coauthors, 2015: Impacts on ocean heat from transient mesoscale eddies in a hierarchy of climate models. *Journal of Climate*, **28**, 952–977, https://doi.org/10.1175/JCLI-D-14-00353.1.

Grist, J. P., S. A. Josey, Y.-O. Kwon, R. J. Bingham, and A. T. Blaker, 2014: The surface-forced overturning of the north Atlantic: Estimates from modern era atmospheric reanalysis datasets. *Journal of Climate*, **27**, 3596–3618, https://doi.org/10.1175/JCLI-D-13-00070.1.

Groeskamp, S., , and D. Iudicone, 2018: The effect of air-sea flux products, shortwave radiation, depth penetration, and albedo on the upper ocean overturning circulation. *Geophys. Res. Lett.*, **45**, 9087–9097, https://doi.org/10.1029/2018GL078442.

Groeskamp, S., S. M. Griffies, D. Iudicone, R. Marsh, A. G. Nurser, and J. D. Zika, 2019: The water mass transformation framework for ocean physics and biogeochemistry. *Annual Review of Marine Science*, **11 (1)**, 271–305, https://doi.org/10.1146/annurev-marine-010318-095421.

Hewitt, H. T., and Coauthors, 2017: Will high-resolution global ocean models benefit coupled predictions on short-range to climate timescales? *Ocean Modelling*, **120**, 120–136, https://doi.org/10.1016/j.ocemod.2017.11.002.

Hieronymus, M., and J. Nycander, 2013: The budgets of heat and salinity in nemo. *Ocean Modelling*, **67**, 28–38, https://doi.org/10.1016/j.ocemod.2013.03.006.

Holmes, R. M., J. D. Zika, and M. H. England, 2019a: Diathermal heat transport in a global ocean model. *J. Phys. Oceanogr.*, **49**, 141–161, https://doi.org/10.1175/JPO-D-18-0098.1.

Holmes, R. M., J. D. Zika, R. Ferrari, A. F. Thompson, E. R. Newsom, and M. H. England, 2019b: Diathermal heat transport in a global ocean model. *Geophys. Res. Lett.*, **46**, 13 939–13 949, https://doi.org/10.1029/2019GL085160.

Holmes, R. M., J. D. Zika, S. M. Griffies, A. M. Hogg, A. E. Kiss, and M. H. England, 2021: Diathermal heat transport in a

global ocean model. *J. Advances in Modelling Earth Systems*, **13**, e2020MS002 333, https://doi.org/10.1029/2020MS002333.

Huang, R. X., 2010: *Ocean circulation: Wind-driven and thermohaline processes*. Cambridge University Press, 791 pp.

Hughes, C. W., J. Williams, A. Blaker, A. Coward, and V. Stepanov, 2018: A window on the deep ocean: The special value of ocean bottom pressure for monitoring the large-scale, deep-ocean circulation. *Prog. Oceanog.*, **161**, 19–46, doi.org/10.1016/j.pocean.2018.01.011.

Hyder, P., and Coauthors, 2018: Critical Southern Ocean climate model biases traced to atmospheric model cloud errors. *Nature Comms*, **9**, 3625–, https://doi.org/10.1038/s41467-018-05634-2.

Iudicone, D., G. Madec, and T. J. MacDougall, 2008a: Water-mass transformations in a neutral density framework and the key role of light penetration. *Journal of Physical Oceanography*, **38**, 1357–1376, https://doi.org/10.1175/2007JPO3464.1.

Iudicone, D., S. Speich, G. Madec, and B. Blanke, 2008b: The global conveyor belt from a Southern Ocean perspective. *Journal of Physical Oceanography*, **38**, 1401–1425, https://doi.org/10.1175/2007JPO3525.1.

Jackson, L. C., and Coauthors, 2020: Impact of ocean resolution and mean state on the rate of AMOC weakening. *Climate Dynamics*, **55**.

Johnson, H. L., P. Cessi, D. P. Marshall, F. Schloesser, and M. A. Spall, 2019: Recent contributions of theory to our understanding of the Atlantic Meridional Overturning Circulation. *J. Geophys. Res. Oceans*, **124**, 5376–5399, https://doi.org/10.1029/2019JC015330.

Kara, A. B., P. A. Rochford, and H. E. Hurlburt, 2000: An optimal definition for mixed layer depth. *J. Geophys. Res.*, **105,C7**, 16,803–16,821.

Kuhlbrodt, T., J. M. Gregory, and L. C. Shaffrey, 2015: A process-based analysis of ocean heat uptake in an AOGCM with an eddy-permitting ocean component. *Clim. Dyn.*, **45**, 3205–3226, https://doi.org/10.1007/s00382-015-2534-0.

Kuhlbrodt, T., and Coauthors, 2018: The low resolution version of HadGEM3 GC3.1: Development and evaluation for global climate. *J. Adv. Model. Earth Sy.*, **10**, 2865–2888, https://doi.org/10.1029/2018MS001370.

Lee, M.-M., A. C. Coward, and A. J. G. Nurser, 2002: Spurious diapycnal mixing of the deep waters in an eddy-permitting global ocean model. *J. Phys. Oceanogr.*, **32,5**, 1522–1535.

Liu, C., and Coauthors, 2015: Combining satellite observations and reanalysis energy transports to estimate global net surface energy fluxes. *J. Geophys. Res. Atmos.*, **120**, 9374–9389, https://doi.org/10.1002/2015JD023264.

Liu, C., and Coauthors, 2017: Evaluation of satellite and reanalysis-based global net surface energy flux and uncertainty estimates. *J. Geophys. Res. Atmos.*, **122**, 6250–6272, https://doi.org/10.1002/2017JD026616.

Luyten, J. R., J. Pedlosky, and H. Stommel, 1983: The ventilated thermocline. *J. Phys. Oceanogr.*, **13**, 292–309.

Madec, G., and Coauthors, 2019: NEMO ocean engine . *Scientific Notes of Climate Modelling Center*, **27**, https://doi.org/10.5281/zenodo.1464816.

Marsh, R., 2000: Recent variability of the north Atlantic thermohaline circulation inferred from surface heat and freshwater fluxes. *J Climate*, **13**, 3239–3260, https://doi.org/10.1175/1520-0442(2000)013,3239:RVOTNA.2.0.CO;2.

Marshall, D. P., and H. L. Johnson, 2013: Propagation of meridional circulation anomalies along western and eastern boundaries. *J Phys. Oceanogr.*, **43,12**, 2699–2717.

Marshall, D. P., D. R. Munday, L. C. Allison, R. J. Hay, and H. L. Johnson, 2016: Gill's model of the antarctic circumpolar current, revisited: The role of latitudinal variations in wind stress. *Ocean Modelling*, **97**, 37–51, https://doi.org/10.1016/j.ocemod.2015.11.010.

McWilliams, J. C., G. Danabasoglu, and P. R. Gent, 1996: Tracer budgets in the warm water sphere. *Tellus*, **48A**, 179–192, https://doi.org/10.3402/tellusa.v48i1.12046.

Minobe, S., A. Kuwano-Yoshida, N. Komori, S. P. Xie, and R. J. Small, 2008: Influence of the Gulf stream on the troposphere. *Nature*, **452**, 206–209.

Munday, D. R., H. L. Johnson, and D. P. Marshall, 2013: Eddy saturation of equilibrated circumpolar currents. *J. Phys. Oceanogr.*, **43**, 507–532.

Murtugudde, R., J. Beauchamp, C. R. McClain, M. Lewis, and A. J. Busalacchi, 2002: Effects of penetrative radiation on the upper tropical ocean circulation. *J. Climate*, **15**, 470–486.

Nikurashin, M., and G. Vallis, 2011: A theory of deep stratification and overturning circulation in the ocean. *J. Phys. Oceanogr.*, **41**, 485–502.

Nurser, A. J. G., and S. M. Griffies, 2019: Relating the diffusive salt flux just below the ocean surface to boundary freshwater and salt fluxes. *J. Phys. Oceanogr.*, **49**, 2365–2376, https://doi.org/10.1175/JPO-D-19-0037.1.

Nurser, A. J. G., R. Marsh, and R. G. Williams, 1999: Diagnosing water mass formation from air-sea fluxes and surface mixing. *J. Phys. Oceanogr.*, **29**, 1468–1487.

Roberts, M. J., and Coauthors, 2019: Description of the resolution hierarchy of the global coupled HadGEM3-GC3.1 model as used in CMIP6 HighResMIP experiments. *Geoscientific Model Development*, **12 (12)**, 4999–5028, https://doi.org/10.5194/gmd-12-4999-2019, URL https://gmd.copernicus.org/articles/12/4999/2019/.

Roullet, G., and G. Madec, 2000: Salt conservation, free surface, and varying levels: a new formulation for ocean general circulation models. *J. Geophys. Res.*, **105, C10**, 23 927–23 942.

Saenko, O. A., J. M. Gregory, S. M. Griffies, M. P. Couldrey, and F. B. Dias, 2021: Contribution of ocean physics and dynamics at different scales to heat uptake in low-resolution AOGCMs . *J Climate*, **34,6**, 2017–2035, https://doi.org/10.1175/JCLI-D-20-0652.1.

Schloesser, F., R. Furue, J. P. McCreary, and A. Timmermann, 2012: Dynamics of the Atlantic Meridional Overturning Circulation. Part 1: Buoyancy-forced response. *Progress in Oceanogr.*, **101**, 33–62.

Srokosz, M., G. Danabasoglu, and M. Patterson, 2021: Atlantic meridional overturning circulation: Reviews of observational and modeling advances - An introduction. *Journal of Geophysical Research: Oceans*, **126, 1**, https://doi.org/10.1029/2020JC016745.

Stommel, H., 1957: A survey of ocean current theory. *Deep Sea Res.*, **4**, 149–184, https://doi.org/10.1016/0146-6313(56)90048-X.

Storkey, D., and Coauthors, 2018: UK global ocean GO6 and GO7: A traceable hierarchy of model resolutions. *Geosci. Model Dev.*, **11**, 3187–3213, https://doi.org/10.5194/gmd-11-3187-2018.

Talley, L. D., 2013: Closure of the global overturning circulation through the Indian, Pacific, and Southern oceans: Schematics and transports. *Oceanography*, **26**, 80–97, https://doi.org/10.5670/oceanog.2013.07.

Talley, L. D., G. L. Pickard, W. J. Emery, and J. H. Swift, 2011: *Descriptive Physical Oceanography*. Elsevier, London, 555 pp.

Tamsitt, V., R. P. Abernathey, M. R. Mazloff, J. Wang, and L. D. Talley, 2018: Transformation of deep water masses along Lagrangian upwelling pathways in the Southern ocean. *J. Geophys. Res. Oceans*, **123**, 1994–2017, https://doi.org/10.1002/2017JC013409.

Tamsitt, V., L. D. Talley, M. R. Mazloff, and I. Cerovecki, 2016: Zonal variations in the Southern ocean heat budget. *J. Climate*, **29**, 6563–6579, https://doi.org/10.1175/JCLI-D-15-0630.1.

Vallis, G. K., 2017: *Atmospheric and Oceanic Fluid Dynamics*. Cambridge University Press, https://doi.org/10.1017/9781107588417.

van Sebille, E., and Coauthors, 2018: Lagrangian ocean analysis: Fundamentals and practices. *Ocean Modelling*, **121**, 49–75, https://doi.org/10.1016/j.ocemod.2017.11.008.

Walin, G., 1982: On the relation between sea-surface heat flow and thermal circulation in the ocean. *Tellus*, **34**, 187–195.